Lawrence Berkeley National Laboratory

Title
Actinic imaging and evaluation of phase structures on EUV lithography masks

Permalink
https://escholarship.org/uc/item/8h288879

Author
Mochi, Iacopo

Publication Date
2010-11-05

Actinic imaging and evaluation of phase structures on EUV lithography masks

Iacopo Mochi[1], Kenneth A. Goldberg[1], Sungmin Huh[2]

[1]Lawrence Berkeley National Laboratory, [2]Samsung Electronics [d]

We describe the implementation of a phase-retrieval algorithm to reconstruct phase and complex amplitude of structures on EUV lithography masks. Many native defects commonly found on EUV reticles are difficult to detect and review accurately because they have a strong phase component. Understanding the complex amplitude of mask features is essential for predictive modeling of defect printability and defect repair. Besides printing in a stepper, the most accurate way to characterize such defects is with actinic inspection, performed at the design, EUV wavelength. Phase defect and phase structures show a distinct through-focus behavior that enables qualitative evaluation of the object phase from two or more high-resolution intensity measurements. For the first time, phase of structures and defects on EUV masks were quantitatively reconstructed based on aerial image measurements, using a modified version of a phase-retrieval algorithm developed to test optical phase shifting reticles.

I. Introduction

Mask defects are one of the main issues of concern for extreme ultraviolet EUV lithography. The development of accurate defect inspection, imaging, and characterization capabilities is essential to understand mask and pattern quality and to evaluate repair efforts. Existing and emerging non-actinic defect review techniques can fail to assess the extent of defects on EUV blank and patterned masks [1] because of the strong wavelength dependence of the mask and defect optical properties in the EUV region. For this reason, with the exception of printing, actinic mask imaging appears to be the most reliable way to predict the effect that defects in the pattern or on the mask blank will have on the printed wafer.

Email: IMochi@lbl.gov

A peculiar class of defects commonly encountered on EUV reticles and blanks are so called phase defects. They usually originate underneath the multilayer and are therefore particularly difficult to inspect and quantify with scanning electron microscopy (SEM), atomic-force microscopy (AFM) or other inspection methods that probe only the surface of the mask. Based on two or more EUV actinic aerial images recorded through focus, it is possible to obtain quantitative information about the complex amplitude of the electric field at each point in the image plane, including phase. For large mask structures, this technique also allows the reconstruction of the mask properties. In this paper we describe the implementation of a phase reconstruction algorithm and its use to quantify the phase component of defects and other mask structures on patterned and blank EUV masks.

A. Phase structures and phase defects

For several lithography generations, masks have been created with phase-shifting structures to achieve a greater degree of pattern control in the aerial image. Similar efforts have been applied to EUV masks, where phase shifting is created by spatially modifying the structure of the multilayer coating, or the topography of the underlying substrate, and thus modifying the reflected light field. [2,3] Phase structures and defects generally manifest themselves in EUV images as intensity distributions that evolve in a characteristic way through focus. The aerial image behavior depends sensitively on the wavelength, partial coherence and numerical aperture of the imaging system.

Phase defects on EUV masks usually originate from alterations in the topological structure of the multilayer coating caused by buried particles, substrate bumps, or pits. They can be distinguished from amplitude defects for their appearance in through-focus image series. While amplitude defects exhibit a symmetrical intensity distribution for positive and negative defocus values as

shown in Fig. 1 (A), phase defects appear bright on one side of focus and dark on the opposite side. Furthermore, they tend to exhibit high contrast out of focus, and when they are small relative to the resolution of the imaging system, they tend to disappear in the focal plane. Pits and bumps can be distinguished qualitatively by eye, noting their opposite through-focus behavior, as shown in Fig. 1 (B, C). In the presence of a pit defect, the optical path difference of the illumination field increases and produces a positive phase difference in the image plane, while bump defect produces a negative phase difference. While the phase information is lost as a detector or photoresist records the image intensity, this behavior signals that the defect's phase is encoded in its through-focus image evolution. We demonstrate that EUV microscopes that record the aerial image with high resolution can be used to reconstruct the complex image amplitudes.

B.   The Actinic Inspection Tool

The SEMATECH Berkeley Actinic Inspection Tool (AIT) is a synchrotron-based Fresnel zoneplate microscope dedicated to EUV mask imaging. The microscope is an all-EUV instrument featuring an array of selectable objective zoneplate lenses with different numerical apertures and magnifications. The illumination wavelength is tunable between 13.2 and 13.6 nm and the partial coherence has been estimated to be $0.15 < \sigma < 0.2$. Detailed descriptions of the AIT and its performance have been published previously [4,5]. For simplicity the AIT can be modeled as a simple on-axis circular lens, with coherent illumination.

To a achieve a higher mechanical stability in recording through-focus series, the AIT's mask and lens positions are not mechanically adjusted during the series. Instead we adjust the focal length of the lens by relying on the zoneplate's chromatic dependence, the narrow illumination

bandwidth ($\lambda/\Delta\lambda = 1450$), and our ability to finely tune the wavelength using the beamline's monochromator. [6] The relationship between the focal length and the wavelength is

$$\lambda\ f = \lambda_0\ f_0. \hspace{6cm} 1$$

By design, $\lambda_0 = 13.4$ nm and $f_0 = 750$ nm; λ and f are the changing wavelength and focal length. Using this technique, we can achieve the necessary focal change (3 µm) using wavelength changes on the order of 0.4%

II. Phase reconstruction algorithm

The problem of phase retrieval from intensity measurements occurs in many different fields, from astronomy to x-ray diffraction microscopy, and it is usually described as the determination of a Fourier-transform pair [g, G] from partial data on either or both functions [7,9]. We consider here an iterative approach based on the Gerchberg-Saxton (GS) algorithm [9]. In its classical implementation the GS algorithm assumes the knowledge of the measured intensity distributions in the image plane and in the pupil plane, and an educated guess of the phase in the image plane. The first step is to generate the complex amplitude in the image plane using the measured image amplitude and a first guess of the phase. (In different strategies, the guess could be all zeros, a random distribution, or an educated guess.) The second step propagates the field back to the pupil plane using a Fourier transform. In the third step, the amplitude of the field in the pupil plane is substituted with the amplitude of the measured pupil image (i.e. the square root of the measured intensity). The fourth step is to propagate the pupil's complex amplitude to the image plane with an inverse Fourier transform. This process is iterated until the intensity calculated in the image plane matches the measured one to a specified threshold.

Obtaining an image of the pupil in the AIT is not practical; therefore we adopted an algorithm that can recover the phase from two images in planes close to focus. Bunau, *et al.* successfully

used this approach to evaluate phase structures on phase shifting masks for optical lithography [10]. In our version of this algorithm, described in Figure 2, we use an image collected in the focal plane (subscript 0) and a second image with a known amount of defocus (subscript 1), and we make use of our knowledge of the numerical aperture of the imaging system to constrain the field in the pupil plane.

We start with a first guess of the phase in the focal plane P_0 and we calculate the amplitude A_0 from the square root of the measured image intensity. This serves as a starting point for the complex amplitude E_0 in the image plane.

$$E_0 = A_0 \exp(iP_0). \qquad\qquad 2$$

We propagate back to the pupil plane with a fast Fourier Transform (FFT), giving us a complex amplitude E_p in the pupil plane.

$$E_p = A_p \exp(iP_p) = \text{FFT}(E_0). \qquad\qquad 3$$

Here we apply the known (binary) pupil function P_f by multiplication, operating like a low-pass filter. This step removes forbidden light energy from the regions where we know the field is zero. By adding a defocus term, d, to the pupil phase, we can propagate to the out of focus image plane with an inverse FFT (IFFT). The defocus term is a second-order approximation to the spherical phase of a wave emanating from the out of focus plane minus the phase of a wave emanating from the in-focus plane.

$$E_1 = \tilde{A}_1 \exp(iP_1) = \text{IFFT}\left(P_f A_p \exp\left[i\left(P_p + d\right)\right]\right). \qquad\qquad 4$$

The peak magnitude of d is proportional to the defocus.

In the defocus plane, we use the a priori knowledge given by the out of focus image, We keep the phase of the field and replace the amplitude of E_1 with the amplitude A_1 obtained from the measured intensity in the out of focus plane.

$$E_1 = A_1 \exp(iP_1).$$ 5

We then propagate E_1 back to the pupil plane, subtracting the defocus term and again applying the pupil function.

$$\tilde{E}_p = A_p \exp(iP_p) = \mathrm{FFT}(E_1),$$ 6

$$E_p = P_f A_p \exp\left[i(P_p - d)\right].$$ 7

Finally we propagate E_p to the focal plane and compare the calculated amplitude $\tilde{A}_0$ with the known amplitude from the first measured image.

$$\tilde{E}_0 = \tilde{A}_0 \exp(i\tilde{P}_0).$$ 8

We iterate this procedure until the RMS difference of the two amplitudes is below an arbitrary threshold.

Minor variations on the procedure, to improve convergence, may include the addition of random phase in one or both of the planes, or the inclusion of information from previous iterations to provide continuity. These ideas are the subject of ongoing research.

III. Simulations

At this time, there is no easy way to verify the phase reconstruction algorithm using real data, because standard mask inspection techniques don't provide direct phase measurements. AFM for example, can be used to measure the surface topography, but the phase effect we are looking for originates in the lower layers of the coating. For this reason we conducted a series of simulations to test the performance limits of the phase reconstruction method. In all of the simulations we

considered a numerical aperture of 0.0875 and a wavelength of 13.4 nm, which correspond to the most common configuration of the AIT. We describe the measured accuracy of the methods in the absence of photon shot noise, followed by calculations in which the discreet number of photons and shot noise were included.

We modeled a simple two-dimensional phase defect with a rotationally symmetric Gaussian profile. The field of the reflected wave is given by:

$$E(x, y) = A(x, y) \exp[-iP(x, y)], \qquad\qquad 9$$

where A is the amplitude and P is the phase function.

In the case of a pure phase defect, we considered a constant unit amplitude, A, and a Gaussian phase profile with peak phase p and full width half maximum 2.3 σ.

$$P(x, y) = p \exp\left[-(x^2 + y^2)/2\sigma^2\right]. \qquad\qquad 10$$

We tested the phase reconstruction algorithm for different phase amplitudes to establish the approximate number of iterations required to obtain given levels of phase-measurement accuracy in the reconstruction, when there is no noise in the input. The image of a sub-resolution phase object has a peak phase difference that is lower than the original objects because of the spatial filtering caused by the imaging system. To reduce this discrepancy, in our simulation we chose a profile width σ = 76.65 nm that corresponds to a defect FWHM that is approximately twice the resolution limit of the AIT. We ran the simulation using the intensity distributions calculated for the focal plane ($\Delta f = 0$) and for a defocus corresponding to a focal shift of 1.6 µm (this is typically equal to three or four focus steps within our series). The accuracy of the reconstruction depends both on the number of iterations used and on the peak phase of the simulated object as shown in figure A. For practical purposes, we limited the number of iterations to $4 \cdot 10^4$. With calculations conducted in this manner, we reached an accuracy of 0.02 rad for a defect with a

peak phase of π. This value is biased by the guess on the initial phase, which we chose to be 0. Using this initial phase guess, defects with a smaller peak phase tend to converge faster. In some cases it is possible to make an educated guess of the peak phase of the structures that we want to reconstruct, and this helps to decrease the convergence time.

Source brightness (or power) is one of the main constraints of EUV actinic mask inspection tools, and it imposes a tradeoff between the measurement speed and the photon noise level in the images.

To probe the exposure level requirements of the method, we studied the effect of photon noise on the phase reconstruction. We simulated images with increasing photon counts, following a Poisson distribution, and we evaluated the error in the reconstructed peak phase for defects with different phase amplitudes. The simulation results are shown in Fig 4. Through-focus image series of defects with a smaller peak phase exhibit a lower contrast and the correspondent phase reconstruction is more sensitive to noise. Figure 5 shows the phase reconstruction of a Gaussian pit defect with a peak phase of $\pi/10$ and an average of 2500 photons per pixel. The error bars represent the RMS error calculated over 200 separate simulations.

IV. Experimental results

We tested the phase reconstruction algorithm using AIT images collected on a phase shifting mask, and images of native defects on a full field patterned reticle. During the reconstruction, we track the progress toward convergence by monitoring the RMS amplitude difference between the known image amplitude, and the one reconstructed after each iteration. The presence of noise in real data makes the choice of a cutoff threshold based on the RMS amplitude difference impractical. For example, a high threshold may not guarantee the proper convergence of the reconstruction; while a low threshold might never be reached due to noise. We decided to iterate

the algorithm until the average change of the RMS amplitude difference was less than an arbitrary value proportional to the average number of counts in the images. We set the value to be equal to 4 times the RMS error expected on the basis of the number of counts per pixel in the images.

An additional error source comes from relative image position uncertainties between the two images used in the reconstruction. The off-axis mask imaging creates a lateral displacement between series images that must be carefully compensated to avoid reconstruction artifacts. Further investigation of the required positioning accuracy is the subject of ongoing research.

A.   *Phase shifting mask*

A phase shifting mask is an ideal object to test the reconstruction algorithm since it features different patterns with the same nominal phase difference and nearly uniform reflectivity across its surface. [3] The reticle we used, provided by GlobalFoundries, was made by etching a pattern into the multilayer surface, to a known depth, in order to generate reflective structures with a phase difference of π. Successive studies showed that the mask was actually under-etched and the resultant phase difference between the patterned and unpatterned regions is lower than the expected value. [11]

For our test we selected an isolated square contact with a size of 500 nm, and an array of 150 nm contacts with a 540 nm pitch. Both objects, from nearby regions on the same mask, are designed to have a negative phase relative to their surrounding areas; locally, they are pillars. For the reconstruction we used one image collected in the focal plane, and second with a defocus of 1.6 µm. As with the simulations, we used a central wavelength of 13.4 nm and a lens with a numerical aperture of 0.0875. The results are shown in Fig. 6(A,B): in the top row (A), you can see two images, in and out of focus, of a square pillar structure with a lateral size of 500 nm and

a nominal phase of $-\pi$. The image on the right shows the complex amplitude. The reconstructed peak phase difference for this structure is -0.74 π. This value is consistent with the fact that the mask was under etched and the expected phase difference value is actually smaller than π. In the middle row (B) you can see the images and the complex amplitude reconstruction of an array of 150 nm square pillars with a 540 nm pitch and the same nominal phase. The average reconstructed peak phase difference for the pillars is -0.53 π. The absolute value of this phase difference is significantly smaller than the one measured for the 500 nm pillar. This can be explained considering the size of these defects and the resolution of the lens used for the measurement. Simulations show that the image of a 150 nm contact with the same phase we measured for the 500 nm pillar, obtained with a NA of 0.0875 and a 13.4 nm wavelength, exhibit a peak phase of 0.60 π.

B.   Native defects

We analyzed a phase defect that we discovered on a clear region of the same phase shifting mask described above. Its through-focus behavior suggests that it is a bump defect. In Fig. 7 we show the two input images that were used, and a longitudinal profile of the reconstructed phase. Our reconstruction shows that the defect has a peak phase of nearly -0.8 rad, consistent with the qualitative evaluation. Accounting for a factor of two in the phase change upon reflection, the single surface approximation [12] would suggest that this defect has an effective height of 6.5 nm. We have not yet performed AFM surface profile measurements for comparison.

Figure 6 also shows a study of a defect found on a full-field, patterned, EUV mask, from GlobalFoundries. [1] This long, narrow defect has a strong phase component in addition to an amplitude change. AFM analysis showed that at its surface, it forms a 20 nm deep, 125 nm wide groove in the multilayer. We used the single surface approximation to evaluate the order of

magnitude of the peak phase in the image plane. Using the NA and wavelength of the AIT we obtained a peak phase of 1.6 π. Our reconstruction, shown in Fig. 6 (B) reveals a peak phase approximately equal to π, consistent with a pit defect with characteristics comparable to the AFM measurement.

V. Conclusions

Our analysis of through-focus imaging data has demonstrated for the first time, that is possible to apply phase reconstruction algorithms to high-resolution EUV aerial image measurements. The complex amplitude (including phase) of defects found on EUV patterned and blank masks, including advanced EUV phase shifting reticles can be calculated based on data from an actinic EUV microscope, like the AIT. Reconstructions can be performed using two intensity measurements, from different focal planes and the known numerical aperture of the imaging system, when the illumination coherence is relatively high. Our simulations reveal that for the noise-free reconstruction of relatively small Gaussian phase defects, the phase-measurement accuracy of the method can be as high as 2 mrad, RMS. In the presence of shot noise, the uncertainty depends on the number of photons and on the peak phase of the image we are trying to reconstruct: for example measure a π/10 nm phase object with an uncertainty of 0.01 rad we need images with an more than 2500 photons per pixel. The measurement of real phase features on a prototype EUV phase-shifting mask showed a satisfactory agreement with the expected.

The phase retrieval technique that we described will deepen our understanding of this class of defects, which are among the most difficult to inspect and characterize. Additional work must be performed to analyze the limiting role of partial coherence on the accuracy of the reconstruction, and study the dependence of image feature size on the defocus step magnitude. Our initial

investigation into the combination of more than two focus series images did not show significant advantage, but more work is clearly needed.

VI. Acknowledgements

References

[1] Mochi, I., Goldberg, K. A., La Fontaine, B.v Tchikoulaeva, A., Holfeld, C., Proc. of SPIE, **7636**, 76361A (2010).

[2] T. Haga, H. Takenaka, M. Fukuda, J. Vac. Sci. Technol. B **18** (6), 2916 (2000).

[3] Bruno La Fontaine, Adam R. Pawloski, Obert Wood, Yunfei Deng, Harry J. Levinson, Patrick Naulleau, Paul E Denham, Eric Gullikson, Brian Hoef, Christian Holfeld, Christian Chovino, Florian Letzkus. Proc. SPIE, **6151**, 61510A (2006).

[4] K. A. Goldberg, P. P. Naulleau, A. Barty, S. B. Rekawa, C. D. Kemp, R. F. Gunion, F. Salmassi, E. M. Gullikson, E. H. Anderson, H.-S. Han, Proc. SPIE **6730**, 67305E(2007);

[5] K. A. Goldberg, P. Naulleau, I. Mochi, E. H. Anderson, S. B. Rekawa, C. D. Kemp, and R. F. Gunion, H.-S. Han, S. Huh , Journal of Vacuum Science and Technology B **26** (6), 2220 (2008).

[6] K. A. Goldberg, I. Mochi, S. Huh , "Collecting EUV mask images through focus by wavelength tuning," SPIE 7271, 72713N-1-8 (2009).

[7] J. Fienup, "Phase retrieval algorithms: a comparison", Applied Optics, **21** (15) pp. 2758-2769 (1992).

[8] R. Barakat, G. Newsam, "Algorithms for reconstruction of partially known, band-limited Fourier-transform pairs from noisy data", J. Opt. Soc. Am. A ,Vol. 2, No. 11 (1985)

[9] R. W. Gerchberg and W. O. Saxton, "A practical algorithm for the determination of the phase from image and diffraction plane pictures," Optik 35, 237 (1972)

[10] R. M. von Bunau, H. Fukuda, and T. Terasawa, Jpn. J. Appl. Phys., Part 1 36, 7494. (1997)

[11] B. La Fonataine, A. R. Pawloski, O. R. Wood II, H. Levinson, P. Denham, E. M. Gullikson, B. Hoef, P. Naulleau, C. Holfeld, C. Chovino, "Printing EUV Phase-Shift Masks using the 0.3 NA Berkeley MET", 4th International EUVL Symposium. (2005)

[12] E. M. Gullikson, C. Cerjan, D. G. Stearns, P. B. Mirkarimi, and D. W. Sweeney, J. Vac. Sci. Technol. B 20, 81 (2002)

Figure 1

Iteration block

Pupil → Apply NA constraint and add defocus

IFFT

FFT

Apply in focus intensity constraint

Out of focus Image → Apply out of focus intensity constraint

Pupil → Apply NA constraint and subtract defocus

IFFT

FFT

In focus Image

Image guess (amplitude and phase)

Reconstructed image (amplitude and phase)
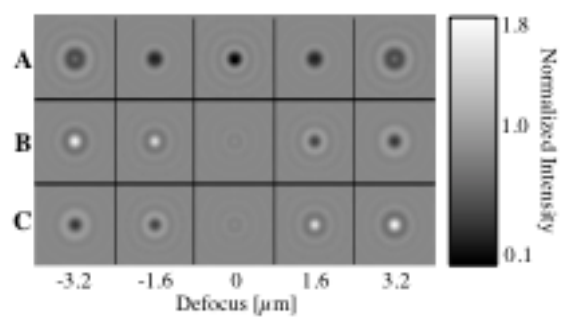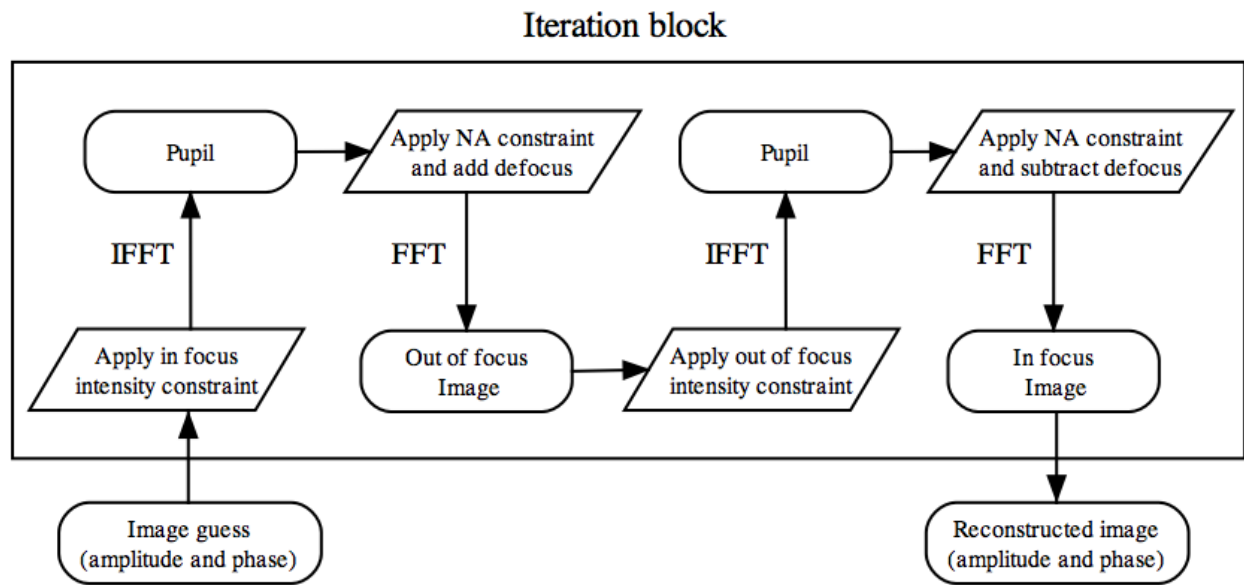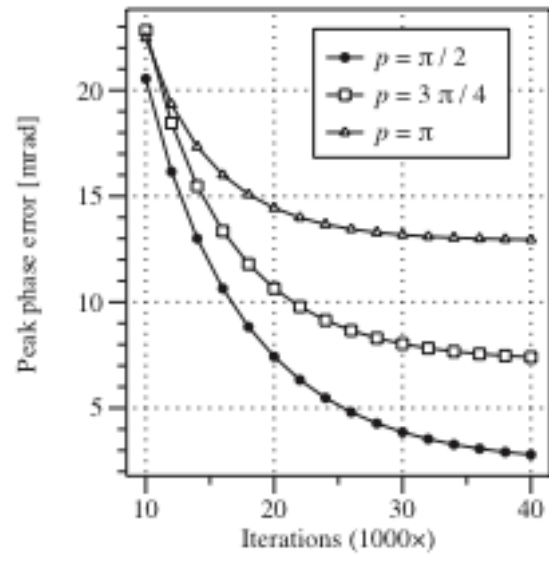
Figure 2

Figure 3

Figure 4

Figure 5

	Intensity ($\Delta f = 0$)	Intensity ($\Delta f = 1.6$)	Complex amplitude
A	0.5 μm contact		
B	150 nm contacts		
C	Defect in 1 μm line		
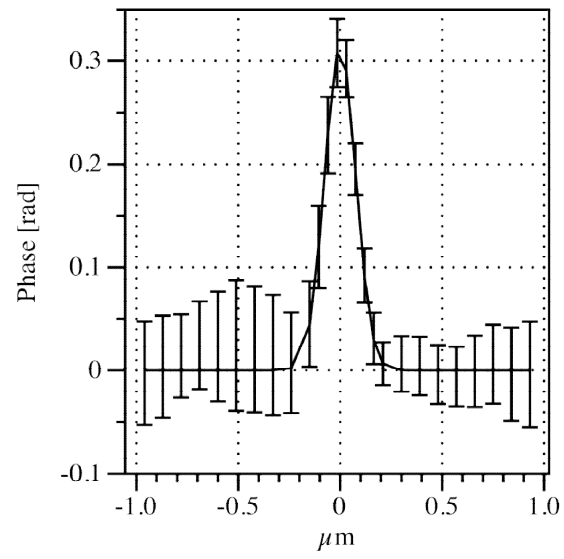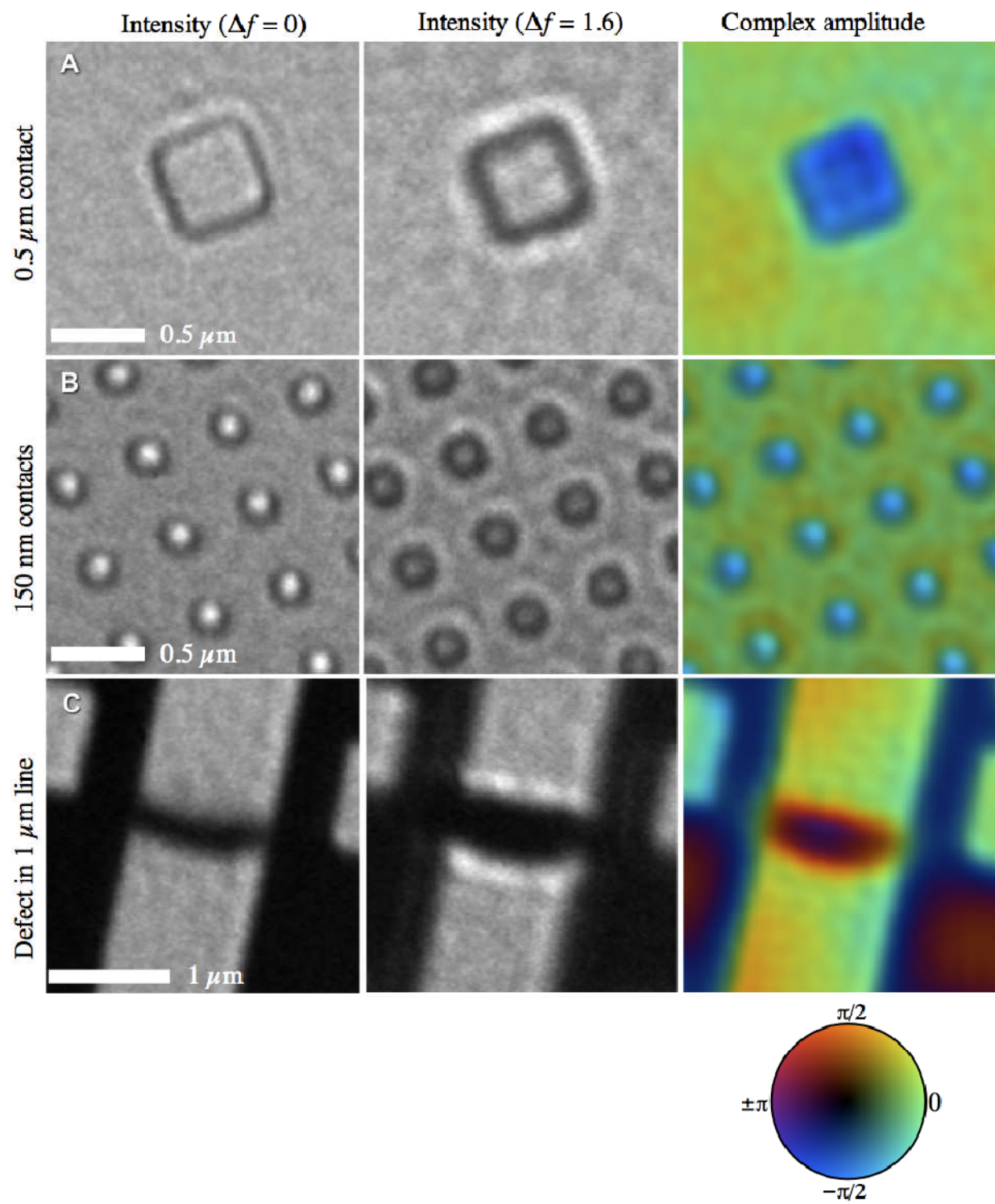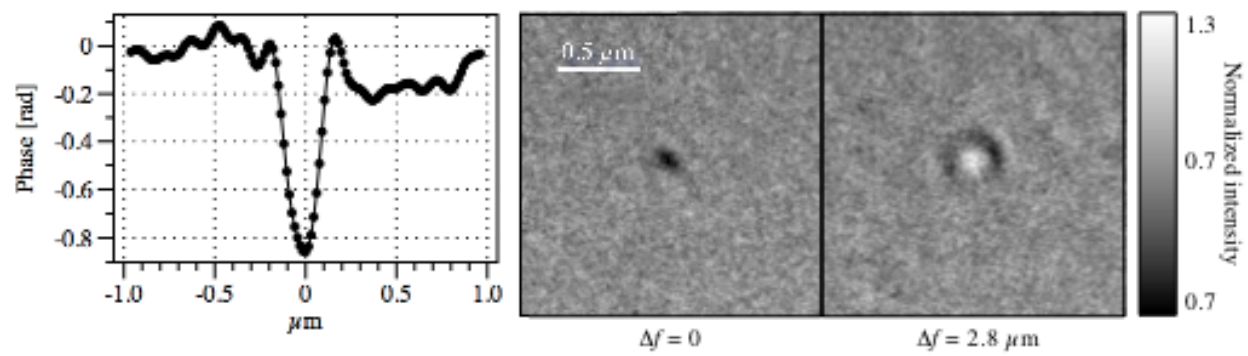
Figure 6

Figure 7

Figure captions

Figure 1. Through focus image simulation of an amplitude defect (A), a phase *bump* (B) and a phase *pit* (C). All the defects have a Gaussian profile either in phase or amplitude and a FWHM of 90 nm. The amplitude of (A) goes from 0 to 1 and the peak phase for B and C is $-\pi/10$ and $\pi/10$ respectively. Each tile is 1.9 µm wide. The NA and the wavelength used for this simulation are 0.0875 and 13.4 nm respectively.

Figure 2. Schematic representation of the GS phase-retrieval algorithm that we employed, modified to work with an image collected in the focal plane and an image with a known amount of defocus.

Figure 3. Phase reconstruction accuracy. The picture shows the difference between the expected and reconstructed peak phase values for three different Gaussian phase defects as a function of the iteration number.

Figure 4. Phase reconstruction of noisy data. The picture shows the reconstructed peak phase RMS error calculated over 200 samples as a function of the number of photons for three different phase defects. We assumed a Poisson distribution for the noise and we run 10^4 iterations for each defect.

Figure 5 Gaussian defect profile reconstruction. The simulated defect has a phase of $\pi/10$ and a FWHM of 180 nm. The average number of photons per pixel in this simulation is 2500 and the error bars are calculated as the RMS error over 200 separated simulations.

Figure 6. Phase reconstruction of PSM structures (A, B) and of native defect on a full field patterned mask (C). In the complex amplitude plots on the right, the phase is represented as hue and the normalized amplitude is shown as color brightness.

Figure 7. Phase reconstruction of an isolated defect on a bright region of a phase shifting mask. The left panel shows the phase profile of the defect.

DISCLAIMER